

Performance of SrBr₂·6H₂O based seasonal thermochemical heat storage in a novel multilayered sieve reactor

Wei Li, Hao Guo, Min Zeng*, Qiuwang Wang

Key Laboratory of Thermo-Fluid Science and Engineering, Ministry of Education, Xi'an Jiaotong University, Xi'an, Shaanxi 710049, China



ARTICLE INFO

Keywords:

Salt hydrate
SrBr₂·6H₂O
Thermochemical heat storage
Multilayered sieve reactor
Thermal performance

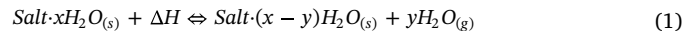
ABSTRACT

The salt hydrate-based thermochemical heat storage (TCHS) system, based on a reversible solid-gas chemical reaction, is currently a key technique used to store heat for later discharge. Strontium bromide hexahydrate (SrBr₂·6H₂O) is one of the most promising candidate materials in seasonal heat storage for residential heating due to its lower desorption temperature. This study develops and numerically investigates a novel multilayered sieve reactor that can promote dehydration and hydration reactions. This paper focuses on the interaction between the porous reactive salt beds and the vapor in an open system. The required time to totally dehydrate and hydrate the salt beds are approximately 1180 min and 940 min, respectively. The effects of various operating conditions such as input temperature, inlet velocity, and relative humidity of fluid on charging and discharging are studied, as well as the influence of thermal conductivity, permeability and kinetic factors. For instance, the reaction kinetic factor $R_{kin} = 1.0 \times 10^{-4}$ is a threshold in this model. The optimized salt beds reduce dehydration time by 11.4% (130 min). High volumetric thermal powers are obtained for the multilayered sieve reactor, although the values decrease with the degree of conversion. The results indicate that the thermal efficiency η , thermal coefficient of performance (COP_{th}), and exergy coefficient of performance (COP_{ex}) of charging are 85.2%, 72.4%, and 21.3%, respectively, and the corresponding values for discharging are 94.5%, 71.5%, and 21.1%, respectively, for the model studied.

1. Introduction

As the energy crisis grows, it becomes indispensable to develop renewable and sustainable energy sources to alleviate energy shortages and global warming. Thermal energy storage (TES), as a potential solution to meet the requirements of energy supply and demand, will play an increasingly crucial role [1,2]. Compared with sensible and latent heat storage, thermochemical heat storage (TCHS) has the benefits of higher heat storage density (about 200–500 kWh m⁻³) [3], negligible heat losses, and most importantly, long-term or seasonal heat storage [2,4,5] due to the conversion between chemical potential and heat energy. As a result, TCHS is considered promising and has received burgeoning attention from researchers. Generally speaking, TCHS includes two types of technology, pure chemical reaction and chemisorption reaction [6]. The former one relies on the occurrence of reversible reactions between two or more separate chemical substances, during which a great amount of heat is absorbed or released. Examples include the oxide/hydroxide reversible reactions of CaO/Ca(OH)₂ [7–9] and MgO/Mg(OH)₂ [10], the metal/metal hydride reaction of Mg/MgH₂ [11,12], steam methane reforming [13], and the redox chemical

reaction of CoO/Co₃O₄ [14]. Heat storage with pure chemical reaction generally requires demanding operations (such as high temperature or high pressure). Furthermore, some reaction processes are complicated or product unfavorable byproducts. In contrast, chemisorption reactions, have a lower activation energy, which makes this technology more feasible than pure chemical reaction at low temperature [15]. The inorganic salt/vapor working pairs, as the typical chemisorption heat storage system, has gradually been favored by researchers in recent years. The salt hydrate utilizes reversible solid-gas reactions to store or release heat during dehydration (charging) or hydration (discharging). The chemical reaction of the salt hydrate is described as follows:



During the heat storage (charging) process, the hydrous salt is heated with heat from a solar thermal collecting device or industrial waste heat until it is anhydrous or less hydrous; that is, water molecules desorb from the salt. Thus, thermal energy is converted into chemical energy and is steadily stored. Discharging occurs once vapor or wet air is applied to the anhydrous salt and re-adsorbs, and the reaction heat is released, as depicted in Fig. 1. The TCHS system based on a hydrous salt

* Corresponding author.

E-mail address: zengmin@mail.xjtu.edu.cn (M. Zeng).

Nomenclature		
A	area of inlet and outlet (m^2)	
A_f	frequency factor (s^{-1})	
B	number of layers of salt bed	
c	concentration of vapor (mol m^{-3})	
C_p	specific heat ($\text{J kg}^{-1} \text{K}^{-1}$)	
COP_{ex}	exergy coefficient of performance	
COP_{th}	thermal coefficient of performance	
D_g	gas diffusivity in porous reactive bed ($\text{m}^2 \text{s}^{-1}$)	
E_a	Arrhenius activation energy (J mol^{-1})	
E_{dm}	mass storage energy density of the salt (J kg^{-1})	
E_x	exergy (J)	
$f(T)$	kinetic rate constant (s^{-1})	
g	acceleration of gravity (m s^{-2})	
$g(p)$	function describing the pressure effect during the chemical process	
h	convective heat transfer coefficient ($\text{W m}^{-2} \text{K}^{-1}$)	
h_0	thickness of the salt beds (cm)	
h_1	distance between salt beds (cm)	
h_a	specific enthalpy of dry air (J kg^{-1})	
h_v	specific enthalpy of water vapor (J kg^{-1})	
$h(X)$	function describing the influence of conversion	
H	enthalpy (J)	
ΔH_r	reaction enthalpy (kJ mol^{-1})	
k	permeability (m^2)	
L	length of the reactor (cm)	
L_0	length of the salt beds (cm)	
M_v	molecular mass of vapor (g mol^{-1})	
M_s	molecular mass of salt (g mol^{-1})	
n	amount of salt that has been involved in the reaction (mol)	
N	steam molar flux ($\text{mol m}^{-3} \text{s}^{-1}$)	
p	pressure (Pa)	
p_{eq}	equilibrium pressure (Pa)	
p_{ref}	reference pressure (Pa)	
p_v	water vapor pressure (Pa)	
P_{ch}	average thermal power during charging (W)	
$P_{ch,v}$	volumetric average thermal power during charging (W m^{-3})	
P_{dis}	average thermal power during discharging (W)	
$P_{dis,v}$	volumetric average thermal power during discharging (W m^{-3})	
\dot{q}	volume power source (W m^{-3})	
Q_{loss}	heat waste to environment (J)	
Q_r	reaction heat (J)	
Q_{rele}	released heat (J)	
Q_{se}	sensible heat (J)	
r	radius of inlet and outlet pipe (cm)	
R	ideal gas constant ($\text{J mol}^{-1} \text{K}^{-1}$)	
R_{kin}	kinetic factor (s^{-1})	
S_w	mass source of water vapor ($\text{kg m}^{-3} \text{s}^{-1}$)	
ΔS_r	entropy of the reaction of dehydration ($\text{J mol}^{-1} \text{K}^{-1}$)	
T	temperature (°C)	
T_{in}	input temperature of discharging (°C)	
T_o	environment temperature (°C)	
t	time (min)	
\vec{u}	velocity vector (m s^{-1})	
v	velocity component (m s^{-1})	
V	volume of salt bed (m^3)	
V_R	volume of reactor (m^3)	
X	reaction conversion (%)	
z	stoichiometric number	
<i>Greek symbols</i>		
ρ	volumetric density (kg m^{-3})	
μ	dynamic viscosity (Pa s)	
σ	ratio between the sensible and the reaction energy (%)	
ε	porosity of the salt bed	
η	thermal efficiency (%)	
λ	thermal conductivity ($\text{W m}^{-1} \text{K}^{-1}$)	
φ	relative humidity (%)	
δ	thickness of adiabatic layer (cm)	
<i>Subscripts</i>		
a	dry air	
ch	charging	
dis	discharging	
eff	effective	
eq	equilibrium state	
ex	exergy	
ext	external environment	
g	gas	
in	inlet or input	
kin	kinetic	
m	moist air	
out	outlet or output	
r	reaction	
ref	reference	
R	reactor	
s	salt or solid grains	
$s0$	dehydrated salt	
$s1$	hydrated salt	
sen	sensible	
$stor$	storage	
th	thermal	
v	vapor	
vip	vacuum insulated panel	

has proven reliable for the micro cogeneration of heat and power (micro-CHP) [16–18] and for domestic application [19,20]. The salt hydrate should meet the requirements of high energy storage density, satisfactory stability, high recyclability, non-toxicity, reasonable price, and easy preparation. The thermochemical materials (TCMs) strongly affect the performance of the TCHS system. Therefore, it is important to investigate TCMs further to develop salt hydrate-based TCHS systems.

N'Tsoukpoe et al. [21] assessed dozens of chemical reactions of salt hydrates to screen them for use in low-temperature TCHS. They found that $\text{SrBr}_2 \cdot 6\text{H}_2\text{O}$ and $\text{LaCl}_3 \cdot 7\text{H}_2\text{O}$ appeared to be the most promising candidates thermodynamically. Li et al. [22] proved that $\text{LiOH}\cdot\text{H}_2\text{O}$ is a prospective TCM for a TCHS system below 373 K by TG-DSC analysis, and its maximum heat storage density is 604 kWh m^{-3} . Brancato et al.

[23] and Van Essen et al. [24,25] analyzed the properties of $\text{MgSO}_4 \cdot 7\text{H}_2\text{O}$, $\text{Al}_2(\text{SO}_4)_3 \cdot 18\text{H}_2\text{O}$, $\text{MgCl}_2 \cdot 6\text{H}_2\text{O}$, and $\text{CaCl}_2 \cdot 6\text{H}_2\text{O}$ from the perspective of heat storage density, reliability, operating conditions, cost, etc. They concluded that these common salt hydrates have potential for application in seasonal household heating. Researchers at the Energy Research Centre of the Netherland [26,27] conducted numerous lab-scale experiments on $\text{MgCl}_2 \cdot 6\text{H}_2\text{O}$, $\text{MgSO}_4 \cdot 7\text{H}_2\text{O}$, and $\text{CaCl}_2 \cdot 2\text{H}_2\text{O}$. Their results indicated that the heat storage density of these hydrates was above 112 kWh m^{-3} (0.4 GJ m^{-3}) and that the dehydration processes occurred step-by-step in different temperature ranges. For example, $\text{MgCl}_2 \cdot 6\text{H}_2\text{O}$ desorbs vapor to form $\text{MgCl}_2 \cdot 4\text{H}_2\text{O}$ at roughly 50–90 °C and to form $\text{MgCl}_2 \cdot 2\text{H}_2\text{O}$ at 90–120 °C for the first and second step, respectively. After that, the vapor is difficult to desorb from

$\text{MgCl}_2 \cdot 2\text{H}_2\text{O}$ and the toxic gas HCl can be generated when the heating temperature is over 140°C , leading to irreversible loss [28]. Sutton et al. [29,30] proposed layering and blending techniques to promote discharge from mixed salts (CaCl_2 , LiNO_3 , and MgSO_4). Their results showed a 24% higher performance when the most efficient heat release strategy was employed, which yielded a heat storage density of 56 kWh m^{-3} . Farcot et al. [31] selected $\text{SrCl}_2 \cdot \text{H}_2\text{O}$ to numerically study the performance of a TCHS system due to the salt's lower operating temperature and good energy density ($\sim 300 \text{ kWh m}^{-3}$). Wyttensbach et al. [32] designed a circular moving bed thermochemical reactor and tested the composite material based on CaCl_2 . The reactor is separated from the TCM storage tanks. A vibrating sieve is used to even the thickness of the solid hydrate bed and to increase the mass transfers with moist air. The experimental results indicated that the moving bed can improve the kinetic properties of adsorption and desorption with an energy density of 200.4 Wh kg^{-3} TCM. Malley et al. [33] numerically studied the influences of the open reactor geometrical features on heat storage process based on the finite element method. The simulated results showed that the reactor with optimized module configuration drastically increased overall performance with less pump power. Marias et al. [34] established a relationship for an open thermochemical system grounded on thermodynamic analysis, the hydration/dehydration cycles of $\text{KAl}(\text{SO}_4)_2 \cdot 12\text{H}_2\text{O}$ and $\text{SrBr}_2 \cdot 6\text{H}_2\text{O}$ were also explored. Among these hydrates, $\text{SrBr}_2 \cdot 6\text{H}_2\text{O}$ is considered a very promising salt hydrate candidate for low-temperature TCHS system [3,21,35], even though it is several times more expensive than others. The ideal energy storage density of $\text{SrBr}_2 \cdot 6\text{H}_2\text{O}$ is 629 kWh m^{-3} (2.27 GJ m^{-3}) [3,4], much greater than other hydrates. A temperature range of $80\text{--}90^\circ\text{C}$ [35] is sufficient to dehydrate from the hexahydrate to the monohydrate without inconsistent dissolution of water vapor in the solid phase. Compared with other hydrates, $\text{SrBr}_2 \cdot 6\text{H}_2\text{O}$ is less prone to excessively adsorb water vapor causing deliquescence or agglomeration. Furthermore, charging (dehydration) temperatures of 60°C [34] and $62\text{--}82^\circ\text{C}$ [36] can be achieved according to the humidity and vapor flow conditions. Michel et al. [36,37] experimentally investigated the open TCHS processes of $\text{SrBr}_2 \cdot 6\text{H}_2\text{O}$ for several months based on the layered packed bed. The reactor was of modular design, stacking eight rectangular modules fed in parallel to improve heat and mass transfer. The maximum hydration specific powers of 2 W kg^{-1} and heat storage density of 203 kWh m^{-3} were obtained, the good cycle performance of the salt was also verified. Fopah Lele et al. [16,18] devised a lab-scale honeycomb reactor and experimentally studied the closed TCHS performance. Their results revealed that the energy density and heat efficiency of the salt bed were 213 kWh m^{-3} and 0.77, respectively. Wang et al. [38,39] developed a composite material ($\text{SrBr}_2 \cdot 6\text{H}_2\text{O} + \text{vermiculite}$) for a low-temperature TCHS and realized a heat discharge power of 67.4 kWh

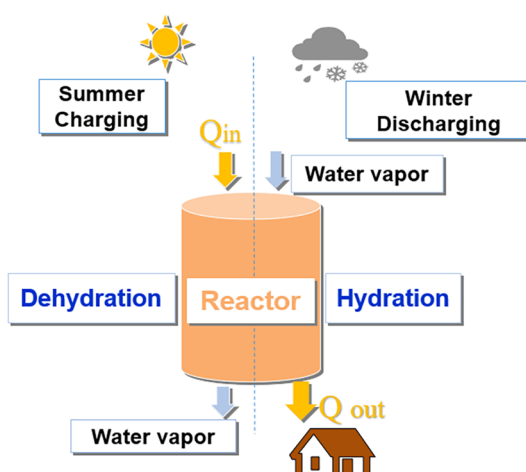


Fig. 1. Schematic of TCHS system for seasonal running.

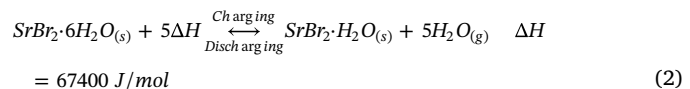
m^{-3} . Analogously, Courbon et al. [40] incorporated $\text{SrBr}_2 \cdot 6\text{H}_2\text{O}$ in a porous silica gel to strengthen the stability of the salt. The composite sorbent eventually yielded an energy storage density of 203 kWh m^{-3} .

It can be seen from previous studies that the performance analyses of salt hydrate-based TCHS have relied primarily on experimentation, and the effect of the reactor configuration on dehydration or hydration has not been sufficiently studied. For those salt candidates, the $\text{SrBr}_2 \cdot 6\text{H}_2\text{O}$ seems to be preferred by scholars and is often selected as the TCM in recent publications due to its merits of greater heat storage density, medium hydroscopic (prevent deliquescence problem), stable properties and low charging temperature ($< 100^\circ\text{C}$) when compared with other salts. Aforementioned reviews also indicate that a modified reactor for enhancing the heat and mass transfer during reaction is indispensable. At the best of authors' knowledge, apart from a few lab-scale reactors described above, there has been little research on reactors for hydrates-based TCHS. Overall, by searching the published literature, it can be found that there are few researches on the reactor used for open hydrous salt heat storage system. Especially for open systems, reactants were usually simply stacked in containers as reaction beds. Therefore, the heat and mass transfer enhancement and compactness are two important factors to consider when designing the reactor. The studies on such reactors are not enough, and it needs to be further studied by researchers. Additionally, compared with the experiment, the simulations on TCHS are relatively fewer and are primarily based on finite element method coupled with user-defined partial differential equation. A novel reactor with multilayered sieves that can facilitate the hydration and dehydration processes of salt hydrates is proposed in this paper. The target of this research is to numerically analyze the influences of operating conditions, such as desorption temperature, on the heat storage process of $\text{SrBr}_2 \cdot 6\text{H}_2\text{O}$ in the reactor. The structural parameters of the reactor are optimized by simulation. The reactor's thermal power, thermal efficiency, and performance are investigated to provide conducive guidelines for a hydrates-based TCHS system.

2. Principle of $\text{SrBr}_2 \cdot 6\text{H}_2\text{O}$ TCHS and physical model description

2.1. Principle of $\text{SrBr}_2 \cdot 6\text{H}_2\text{O}$ TCHS

The solar or industrial waste heat that acts as a heat source is reserved in the TCHS system by converting the thermal energy into chemical potential, while the TCM is changed from the hexahydrate to the monohydrate state. Conversely, when vapor or moist air is applied to the dehydrated salt bed, heat is released with the occurrence of a hydration reaction. This reversible chemical reaction is described as follows:



Between the heat storage and release periods, the reactor is closed and separated from the reactive gas, preserving the reaction heat with low energy loss over a long time. Therefore, a thermochemical process is quite suitable for seasonal heat storage. No consensus exists on the exact temperature that causes desorption from $\text{SrBr}_2 \cdot 6\text{H}_2\text{O}$ to $\text{SrBr}_2 \cdot \text{H}_2\text{O}$. According to prior researches, the temperature range is $62\text{--}117^\circ\text{C}$ [35,36,38], the difference in desorption temperature may be caused by different operating conditions. Nevertheless, $\text{SrBr}_2 \cdot 6\text{H}_2\text{O}$ is the material that easily loses water molecules when heated and is one of the most promising salt candidates for low-temperature TCHS.

2.2. Physical model description

A 3D cubic reactor model, in which several metal sieve-plate reactive beds are inserted is established as a modelling domain, as shown in Fig. 2(a) and (b). The upper and lower ends of the reactor each have a cylindrical tube as gas inlet and outlet, respectively. Inside the shell,

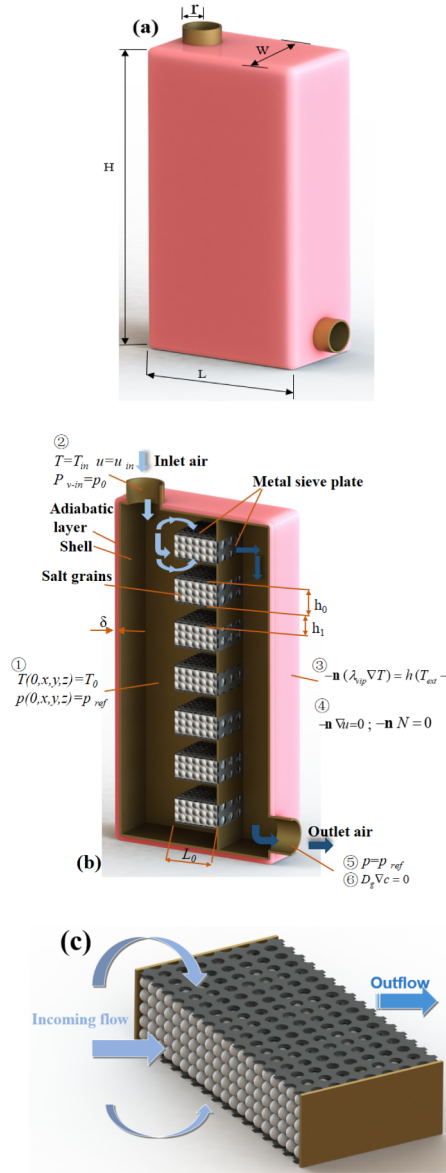


Fig. 2. Schematic diagrams of (a) the overall appearance of the reactor, (b) a symmetrical profile, and (c) an enlarged reaction unit.

each of two metal sieve plates constitutes a reactive bed that is packed with salt-hydrate grains (grain size over 100- μm). The mesh holes of the sieve plate are small enough (tens of microns scale) to prevent leakage of the grains, and the porosity of the sieve is sufficient to guarantee the regular reaction between the inflow gas and solid grains. The width of the reactive bed is the same as that of the reactor housing. In the interior vertical direction of the salt-packed bed, the sieve also serves as the gas outlet of the reactive bed. As a result, the inflow gas can react sufficiently with the three surfaces of each salt-packed bed, that is, the front, the upper, and the lower surfaces. The fluid that experienced dehydration or hydration reaction eventually penetrates the reactive bed and flows out through the vertical mesh sieve (Fig. 2(c)). Note that the sizes of the salt-hydrate grains and the mesh holes in Fig. 2 are not to scale. The periphery, top and bottom, of the reactor shell is covered with a layer of vacuum insulated panel to reduce heat loss during charging or discharging.

Compared to the traditional bulk-packed TCHS reactor, the advantage of this reactor structure is that the incoming gas and the layered reactive beds can exchange heat sufficiently and can evacuate the vapor that is generated vapor during charging in a timely manner to

Table 1
The parameters of the reactor and salt bed.

Parameters	Value
The height of the reactor H (cm)	30
The length of the reactor L (cm)	14
The width of the reactor W (cm)	8
The radius of inlet and outlet pipe r (cm)	1.5
The number of layers of salt bed B	7
The length of salt beds L ₀ (cm)	4
The thickness of the salt beds h ₀ (cm)	2
The distance between salt beds h ₁ (cm)	2
The thickness of adiabatic layer δ (cm)	1

perpetuate the reaction. Moreover, adverse phenomena that may occur in practice, such as the hindrance of heat and mass transfer, or the deliquescence or agglomeration of grains caused by excessive absorption of water vapor, can be effectively avoided due to the small, layered cell. Table 1 lists the reference parameters of the reactor.

3. Theoretical modeling

3.1. Assumption

The present study adopts some assumptions to develop the governing equations describing the mass and energy balances:

- (1) The salt hydrate reactive beds are fixed porous layers, and the porosity is spatially homogeneous and invariable.
- (2) The amount of salt hydrate accumulated on each sieve reactive bed is equal and the influence of the sieve on the solid-gas reaction is neglected.
- (3) The gas is regarded as an ideal gas due to the low concentration of mixed water vapor.
- (4) The local thermal equilibrium between the solid and gas in the porous salt bed is assumed [4,16,33] and the thermal radiation is ignored owing to the relatively low operating temperature (below 100 °C) and the small temperature difference [17,41].
- (5) The gas velocity in the reactive beds follows Darcy's law [16,33], and the reaction enthalpy, ΔH_r , is constant.

3.2. Governing equations

3.2.1. Reaction kinetics

Based on the literature [4,17,42], the reaction kinetics of solid-gas is primarily determined by three major variables: temperature T , pressure p and extent of conversion X . The reaction rate is described as follows:

$$\frac{\partial X}{\partial t} = R_{kin} \cdot (1 - X) \cdot (1 - \frac{P_v}{P_{eq}}) = A_f \cdot \exp(-\frac{E_a}{RT}) \cdot (1 - X) \cdot (1 - \frac{P_v}{P_{eq}}) \quad (3)$$

where R_{kin} is the kinetic factor related to temperature; P_v and P_{eq} are the local partial and equilibrium pressures of water vapor, respectively; A_f is the pre-exponential Arrhenius factor considering the kinetic effect and it is measured by experimentation with a specific reaction system; E_a is the Arrhenius activation energy, and X is the extent of conversion at a given time t .

In the solid-gas chemical reaction of SrBr₂ salt-hydrate, the equation connecting the equilibrium pressure and the temperature is a Clausius–Clapeyron relationship when the equilibrium state can be achieved at the prevailing temperature with an adequately high rate in the mass transfer and chemical reaction [4,16,17]:

$$\ln(\frac{P_{eq}}{P_{ref}}) = -\frac{\Delta H_r}{RT_{eq}} + \frac{\Delta S_r}{R} \quad (4)$$

where P_{ref} , ΔS_r , and R represent the reference pressure, reactive entropy, and universal gas constant, respectively.

3.2.2. Mass conservation and mass transport

To describe the mass balance of this solid-gas reversible reaction, the charging (dehydration) process is selected to illustrate the reaction mechanism. During charging, the decrease in hexahydrate mass density leads to an increase in the mass density of monohydrate and vapor. The density equation is switched into a concentration equation in Comsol for the simulation. Mass transfer in the gas phase takes place via convection as well as diffusion. The mass source the chemical reaction. Therefore, the continuity equations of the solid salt and gas can be written as follows:

$$(1 - \varepsilon) \frac{\partial \rho_s}{\partial t} = \rho_s \frac{\partial X}{\partial t} \quad (5a)$$

$$\varepsilon \frac{\partial \rho_v}{\partial t} = S_w - \nabla(\rho_v \vec{u}) + D_g \Delta \rho_v \quad (5b)$$

where ε is the porosity of the salt bed, and D_g is the water vapor diffusion coefficient in the porous salt bed. The mass source S_w can be expressed as:

$$S_w = z \rho_s \frac{\partial X}{\partial t} \frac{M_v}{M_s} \quad (6)$$

where z is the stoichiometric number of the reaction. M_v/M_s is the ratio of the molecular mass of vapor on molecular mass of solid state. Besides, for the moist air mixture, the mass conservation equation can be written as:

$$\frac{\partial}{\partial t} (\varepsilon \rho_m) + \nabla(\rho_m \vec{u}) = S_w \quad (7)$$

where the ρ_m is the density of mixed moist air.

The Brinkman–Forchheimer extended Darcy model is used to describe the flow in the porous salt beds:

$$\begin{aligned} & \frac{\partial}{\partial t} (\rho_m \vec{u}) + \left(\frac{\vec{u}}{\varepsilon} \nabla \right) (\rho_m \vec{u}) \\ &= \nabla \left[-\varepsilon \vec{p}_v I + \mu_m (\nabla \vec{u} + (\nabla \vec{u})^T) - \frac{2}{3} \mu_m (\nabla \cdot \vec{u}) I \right] + S_w \frac{\vec{u}}{\varepsilon} - \varepsilon \frac{\mu}{k} \vec{u} \end{aligned} \quad (8)$$

where k is the permeability of the porous salt-hydrate bed, μ_m is the viscosity of the water vapor, and g is the acceleration of gravity. The value of the permeability varies in the literature due to the various empirical formulas the different authors adopted. This study uses one set of values [43], the permeability of hydrated salt is $k = 3.1 \times 10^{-11} \text{ m}^2$ and that of the dehydrated salt is $k = 0.7 \times 10^{-10} \text{ m}^2$ for simulation.

3.2.3. Energy conservation equation

The reactive heat is transferred by conduction and convection in the TCM medium. According to the assumptions, the local thermal equilibrium (LTE) exists in the porous salt bed ($T_s \approx T_v = T$). The energy balance equation thus can be expressed as:

$$(\rho C_p)_{\text{eff}} \frac{\partial T}{\partial t} = \nabla(\lambda_{\text{eff}} \nabla T) - C_{pv} \rho_v \vec{u} \cdot \nabla T + \dot{q} \quad (9)$$

where $(\rho C_p)_{\text{eff}} = (1 - \varepsilon)(\rho C_p)_s + \varepsilon(\rho C_p)_v$, and the effective thermal conductivity of the reactive bed $\lambda_{\text{eff}} = (1 - \varepsilon)\lambda_s + \varepsilon\lambda_v$. The λ_s and λ_v are the thermal conductivity of the solid salt and vapor, respectively.

For solid reactive salt, the physical property parameters are related to the degree of reaction. During charging, for instance, the relationship can be written as follows:

$$(\rho C_p)_s = (1 - X)(\rho C_p)_{s1} + X(\rho C_p)_{s0} \quad (10)$$

$$\lambda_s = (1 - X)\lambda_{s1} + X\lambda_{s0} \quad (11)$$

where the subscripts $s1$ and $s0$ refer to hexahydrate and monohydrate, respectively.

In Eq. (9), \dot{q} is the energy source term owing to the hydration (+) or

the dehydration (−) reaction:

$$\dot{q} = \pm \frac{\rho_s}{M_s} \frac{\partial X}{\partial t} \Delta H_r \quad (12)$$

where the sign \pm depends whether it is hydration or dehydration.

3.3. Initial and boundary conditions

In order to clearly describe the initial and boundary conditions in the schematic diagram, Fig. 2(b) is numbered, the numbers and conditions are corresponding in sequence. Temperature and pressure are considered to be functions of time and position in 3-D space as $T = T(t, x, y, z)$ and $p = p(t, x, y, z)$. Additionally, the temperature, pressure, extent of conversion, gas velocity and concentration of vapor in any position inside the reactor are considered to be initially uniform (No.1, as shown in Fig. 2 (b)):

$$T(0, x, y, z) = T_0; \quad p(0, x, y, z) = p_{\text{ref}}; \quad \vec{u} = 0; \quad c = 0; \quad X = 0 \quad (13)$$

At the inlet, the temperature, velocity, and the partial pressure of the water vapor of the inflow gas are constant (No. 2):

$$T = T_{in}; \quad u = u_{in}; \quad p_{v,in} = p_0 \quad (14)$$

The outer wall of the reactor is cooled by the external environment, and thus a convective heat flux exist on the boundary (No.3):

$$-\mathbf{n}(\lambda_{vip} \nabla T) = h(T_{ext} - T) \quad (15)$$

where λ_{vip} and h are the thermal conductivity of the vacuum insulated panel and the convective heat transfer coefficient, respectively.

A non-slip boundary condition was applied at the wall of the shell (No.4). The velocity and species transport acting on the reactor wall therefore can be written as:

$$-\mathbf{n} \nabla u = 0; \quad -\mathbf{n} N = 0 \quad (16)$$

where N is the steam molar flux.

The pressure is external environment pressure, and the temperature gradient is zero at the outlet (No.5):

$$-\mathbf{n}(\lambda \nabla T) = 0; \quad p = p_{\text{ref}} \quad (17)$$

The mass flow through the outlet boundary is considered to be dominated by convection, and thus any mass flux across this boundary due to diffusion is zero (No.6):

$$D_g \nabla c = 0 \quad (18)$$

3.4. Mesh independence test

In this study, the governing equations coupled with the initial and boundary conditions mentioned above were solved by COMSOL Multiphysics 5.4 software using the finite element method, and the partial differential equations were discretized by expansions of Taylor series [17]. Detailed analysis of meshing has been described in our previous research [5] and only a brief description is provided here. An unstructured grid composed of triangular, tetrahedral, pyramid, prism, quadrilateral, vertex, and edge elements was employed. The mesh was partial manually adjusted based on the creation by default. For balancing the accuracy of results with the efficiency of computing, four cases with different cell numbers were selected and compared: coarser mesh (179,968 elements), coarse mesh (361,155 elements), normal mesh (651,766 elements) and fine mesh (1,691,012 elements). The variations of the gas velocity in reactor and bed temperature at a given time are shown in Table 2. No remarkable differences in results between the normal mesh (651,766 elements) and fine mesh (1,691,012 elements) whereas the latter consumed more than triple computation time. Therefore, the normal mesh is employed in this work. The figure showing the half of the symmetrical 3D meshed reactor geometry is

Table 2

The variations of gas velocity and temperature with grid number.

Sequence number (n)	1	2	3	4
Number of grid cells	179,968	361,155	651,766	1,691,012
Velocity (m/s)	0.0605	0.0650	0.0693	0.0697
Change rate of velocity, $(v_n - v_{n-1})/v_{n-1}$	—	7.40%	6.67%	0.59%
Temperature (°C)	74.02	75.79	76.68	76.87
Change rate of temperature, $(T_n - T_{n-1})/T_{n-1}$	—	2.234%	1.174%	0.249%

presented in Fig. 3. The time-scale of 85 000 s with a time step of $\Delta t = 100$ s is selected in the unsteady-state numerical calculations, and the relative tolerance is 0.001. In Comsol Multiphysics, the backward differentiation formula is used for the time stepper and the iterative method adopted by solver is the generalized minimal residual method.

3.5. Model validation

To validate the correctness of the simulation methods used in this research, two lab-scale TCHS experiments from previous investigations were chosen. One is $\text{SrBr}_2\cdot 6\text{H}_2\text{O}$ in a closed honeycomb bed reactor in Ref. [18]. The other is $\text{MgCl}_2\cdot 6\text{H}_2\text{O}$ which was packed in a cylindrical container in Ref. [44]. In Ref. [18], the temperature of the honeycomb reaction bed and the pressure of water vapor were investigated in detail. In Ref. [44], the authors selected $\text{MgCl}_2\cdot 6\text{H}_2\text{O}$ as the TCM to explore its characteristics of heat storage. The experimental results showed that the salt hydrate was decomposed into $\text{MgCl}_2\cdot 4\text{H}_2\text{O}$ and $\text{MgCl}_2\cdot 2\text{H}_2\text{O}$ step-by-step at different temperature ranges when being heated.

The reason for choosing $\text{MgCl}_2\cdot 6\text{H}_2\text{O}$ is that this salt hydrate has been widely investigated for thermochemical heat storage. Therefore, it is representative to simulate the $\text{MgCl}_2\cdot 6\text{H}_2\text{O}$ based heat storage experimental process. Besides, the inlet air with higher temperature was used both in their experiment and the present study to heat the salt grains.

The evolution of the average temperature and pressure in Ref. [18] and the temperature trend in Ref. [44] during dehydration of the salt hydrates were simulated using the methods mentioned in Section 3.4. The simulation results revealed good agreement with the experimental data with a little deviation, as shown in Fig. 4. The maximum relative deviations are 4.65% and 3.42% respectively when the simulation results are compared with the experimental data in Ref. [18] and Ref. [44]. The above two test problems combined together not only indicate that the theoretical model and the assumptions (such as the handling of heat source and the heat transfer in porous medium) we used are reliable, but also validate that the parameters of $\text{SrBr}_2\cdot 6\text{H}_2\text{O}$ and the methods used for simulating the salt hydrate based thermochemical heat storage are convincing.

4. Results and discussion

In numerical simulation, the effects of the structural parameters of the layered sieves reactive bed, the operating conditions, and the physical parameters of reactive salt on the $\text{SrBr}_2\cdot 6\text{H}_2\text{O}$ -based heat storage and release were investigated. The primary reference parameters of the reactor and the thermophysical and other parameters involved in the simulation are listed in Tables 1 and 3. The performance of the charging and discharging of $\text{SrBr}_2\cdot 6\text{H}_2\text{O}$ in the multilayered sieve reactor was analyzed. The Non-isothermal Flow (heat transfer in porous media coupled fluid flow) and partial differential equation (PDE) with user defined functions are adopted and used to solve heat transfer and reaction kinetics, their outputs are the temperature of beds, extent of conversion (here, X is a dimensionless variable between 0 and 1), etc. Therefore, the temperature and extent of conversion of the reaction salt

can be determined at any moment during reaction.

4.1. Dehydration for charging

4.1.1. Temperature profile of reactive bed and flow field of air

During charging, dry and hot air ($T_{in} = 85^\circ\text{C}$) enters the reactor from the inlet with a specific velocity to heat the porous reactive beds. The solid grains absorb heat and subsequently enhance the temperature, and the desorption of water vapor occurs. Fig. 5 displays the average temperature trend of the seven reactive beds (from top to bottom), and Fig. 6 shows the temperature distributions of the reactive beds (half of symmetric geometry) at a given time. Fig. 5 reveals that the temperatures of the reactive beds rise rapidly at first and then experience a gradual rise until the beds temperatures approach the incoming flow temperature. The reason for the varying rate is that the temperature difference between the hot air and the reactive beds is initially greater, and thus, the temperature of the salt increases more rapidly. As the endothermic reaction progresses, the heat absorbed by the reactive salt increases, and as a result, the bulk temperature increases more slowly.

An interesting phenomenon seen in Figs. 5 and 6 is that among the reactive beds, the bed with the fastest temperature rise is neither the bed closest to the inlet nor the one closest to the outlet. The sixth salt bed has a higher temperature than the others followed by the fifth and seventh, successively. The temperature of the one closest to the inlet is the lowest, although the temperature difference among them is inconspicuous. This phenomenon can be attributed to the imbalanced distribution of inlet hot air in reactor. The lower part of the reactor possesses more hot fluid, as a result, the reactive beds at the lower part accordingly absorb more heat than that of the upper beds. Fig. 7 further exhibits the distributions of the flow field, the pressure drop, and the air temperature. The velocity of the inlet fluid decreases due to the larger space, and hot-air continues to flow down until the velocity is very slow, further transfers the heat to the solid grains. Because of this phenomenon, the reactive beds should have a layout in the reactor that allows them to exchange heat with the hot air efficiently. This layout is simply examined in the following section.

4.1.2. Kinetics model of $\text{SrBr}_2\cdot 6\text{H}_2\text{O}$ thermal decomposition

During charging and discharging, the fluid flow, heat transfer, and chemical reaction are coupled and interacting with each other, and the reaction kinetics is of great significance to the chemical reaction process. Fig. 8 reveals the thermal decomposition kinetics of $\text{SrBr}_2\cdot 6\text{H}_2\text{O}$ to

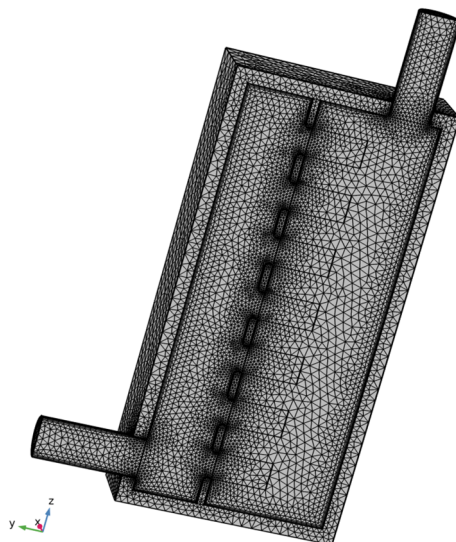


Fig. 3. Half of the symmetrical 3D meshed reactor geometry.

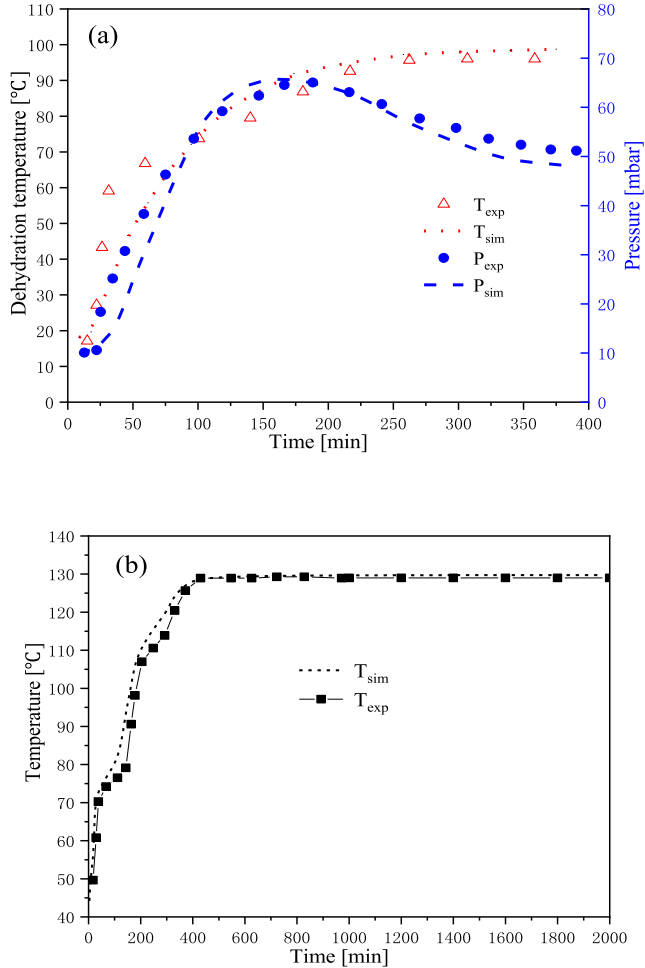


Fig. 4. Comparison of the results between simulation and experimental data: (a) Ref. [18], and (b) Ref. [44].

$\text{SrBr}_2\text{H}_2\text{O}$. The reaction kinetics increases drastically at first, and after 70 min, it gradually declines until the end of desorption. As analyzed in Section 3.2.1, the reaction kinetics is related to the heating temperature, extent of conversion, and vapor pressure, and can be roughly written as follows:

$$\frac{\partial X}{\partial t} = f(T) \cdot h(X) \cdot g(p) \quad (19)$$

The variation in the reaction kinetics result from comprehensive competition among these three aspects. For instance, the conversion of desorption $h(X) = 1 - X$, tends to decrease until it reaches zero, i.e., when the reaction is complete. For the pressure term, $g(p) = 1 - p_v/p_{eq}$, the vapor pressure of p_v is derived from the desorbed steam, and the quickly generated water vapor pulls down the pressure term and accordingly decreases the reaction kinetics. Therefore, it is necessary to evacuate the vapor timely to maintain the reaction continuity.

Fig. 9 shows the average conversion rate of salt-hydrate desorption and the average temperature over time in the charging process, i.e. the extent of reaction and temperature presented in Fig. 8 are average values of the seven bed volumes. Apparently, the bed temperature of the reactive bed increases rapidly, and the desorption conversion is less than 0.05 during this time due to the storage of sensible heat of salt-hydrate. After that, (i.e., when the temperature of the bulk $\text{SrBr}_2\text{H}_2\text{O}$ increases above 60 °C), the salt dehydrates further, and the rate of the temperature rise is restrained owing to the endothermal reaction. Fig. 9 also indicates that the time required to totally dehydrate the bed at a large scale is approximately 1180 min ($X \sim 0.99$). The conversion and vapor pressure distributions of reactive beds at different times are

Table 3

The properties of TCHS system used in numerical simulation [4,16,35,42,43].

Parameters	Description	Value
M_v	Molecular mass of vapor (g mol^{-1})	18.02
M_{s1}	Molecular mass of $S1$ (g mol^{-1})	355.49
M_{s0}	Molecular mass of $S0$ (g mol^{-1})	265.44
C_{ps1}	Specific heat of $S1$ ($\text{J kg}^{-1} \text{K}^{-1}$)	967
C_{ps0}	Specific heat of $S0$ ($\text{J kg}^{-1} \text{K}^{-1}$)	456
C_{vip}	Specific heat of vip ($\text{J kg}^{-1} \text{K}^{-1}$)	1280
λ_{s1}	Thermal conductivity of $S1$ ($\text{W m}^{-1} \text{K}^{-1}$)	0.71
λ_{s0}	Thermal conductivity of $S0$ ($\text{W m}^{-1} \text{K}^{-1}$)	0.56
λ_{vip}	Thermal conductivity of vip ($\text{W m}^{-1} \text{K}^{-1}$)	0.004
ρ_{s1}	Density of $S1$ (kg m^{-3})	2390
ρ_{s0}	Density of $S0$ (kg m^{-3})	3480
ρ_{vip}	Density of vip (kg m^{-3})	240
k_{s1}	Permeability of $S1$ (m^2)	$3.1 \cdot 10^{-11}$
k_{s0}	Permeability of $S0$ (m^2)	$0.7 \cdot 10^{-10}$
$T_{in, ch}$	Input temperature of charging (°C)	85
$T_{in, dis}$	Input temperature of discharging (°C)	20
$T_{o, ch}$	Environment temperature in charging (°C)	30
$T_{o, dis}$	Environment temperature in discharging (°C)	10
P_{ref}	Reference pressure (pa)	101,325
P_o	Partial pressure of water vapor (pa)	340
D_g	Gas diffusion coefficient ($\text{m}^2 \text{s}^{-1}$)	$2.82 \cdot 10^{-5}$
u_{in}	Velocity of inlet air (m s^{-1})	0.5
ε	Porosity	0.8
A_f	Frequency factor in Arrhenius' equation (s^{-1})	16,300
E_a	Activation energy (kJ mol^{-1})	55
R	Ideal gas constant ($\text{J mol}^{-1} \text{K}^{-1}$)	8.314
ΔH_r	Reaction enthalpy (kJ mol^{-1})	337
ΔS_r	Reaction entropy ($\text{J mol}^{-1} \text{K}^{-1}$)	875
h	Convective heat transfer coefficient ($\text{W m}^{-2} \text{K}^{-1}$)	4
z	stoichiometric number	5

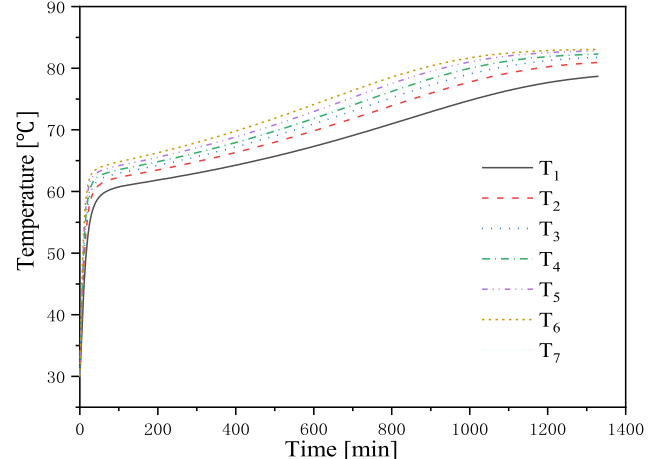


Fig. 5. Temperature of reactive beds vs. time during charging.

shown in Fig. 10. Corresponding to the temperature distribution analyzed above, the lower reactive beds have greater conversion rates. As the reaction progresses, the amount of water vapor desorption decreases. Therefore, the vapor pressure is lower in the later stages of the reaction.

4.2. Hydration for discharging

In contrast to the desorption process, the cold air with a certain humidity is pumped into the salt bed to hydrate it meanwhile the reaction heat is released. The warmer air from the outlet can be used for household heating. Fig. 11(a) exhibits the change in temperature of the reactive beds during discharge. Contrary to charging, the beds located in the lower part of the reactor have lower temperatures, due to the greater incoming flow of cold fluid through the lower beds. Accordingly, more reaction heat is taken away.

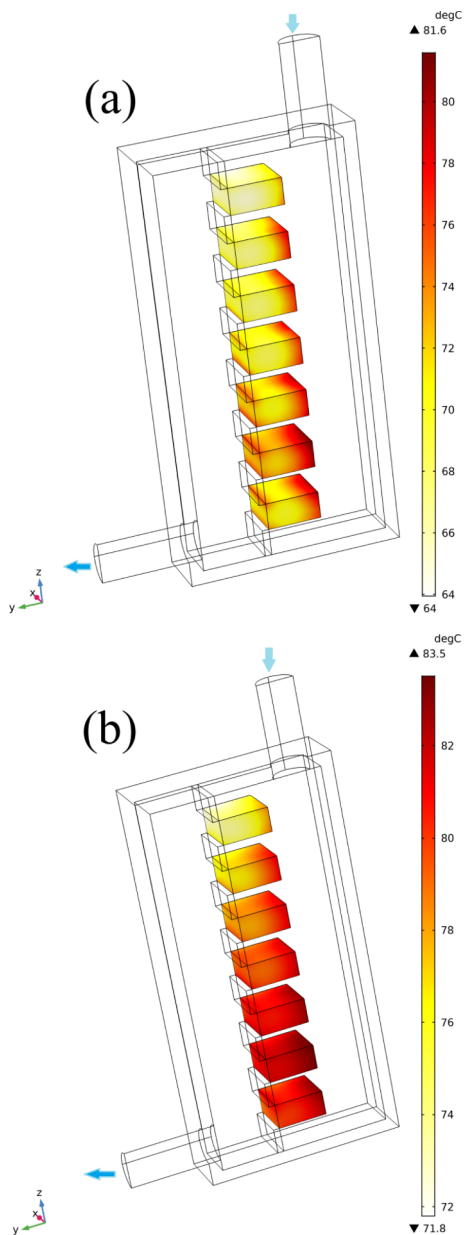


Fig. 6. Temperature distributions of reactive beds at (a) 600 min. and (b) 1000 min. during charging.

The average conversion degree and temperature of $\text{SrBr}_2 \cdot 6\text{H}_2\text{O}$ in the multilayered sieve beds and the outlet temperature over time during discharge are depicted in Fig. 11(b). The time required to completely hydrate the beds is approximately 940 min, shorter than that of dehydration. The outlet temperature of the multilayered sieve reactor is slightly lower than that of the bulk salt, and the peak temperatures are $\sim 33^\circ\text{C}$ and 37°C , respectively.

4.3. Effect of operating conditions

The initial conditions and parameters of the reactive salt have various effects on hydration and dehydration. These conditions should be selected reasonably to meet the system's requirements in practice.

4.3.1. Effect of inlet air

One of the advantages of $\text{SrBr}_2 \cdot 6\text{H}_2\text{O}$ compared to other salt-hydrates is the lower charging temperature (below 100°C). A higher charging temperature and inlet velocity (or volume flow) result in faster

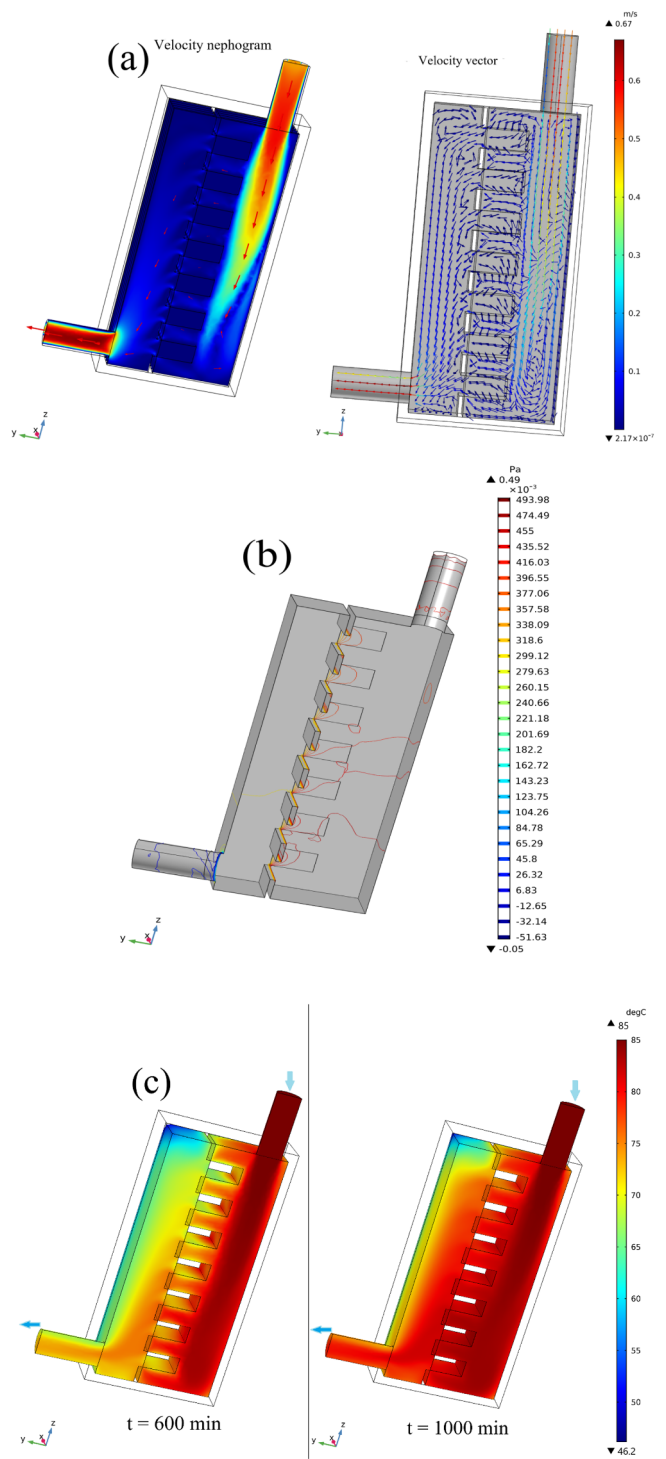


Fig. 7. (a) Velocity and (b) pressure drop of fluid at 10 min, and spatial distributions of the air temperature during charging.

conversion rates (ignoring the occurrence of melting) but may also lower the heat or exergy efficiency (as discussed in Section 4.5). The conversions with different inlet temperatures and velocities in charging are shown in Fig. 12. The time required to complete the desorption process decreases with increased input temperature: the times are around 1380 min, 1180 min, 1010 min, and 880 min as temperature increased. The shortened times gradually decreased for the same temperature difference: the times are 200 min, 170 min, and 130 min. The results highlight the fact that merely enhancing the inlet temperature might not bring maximum economic efficiency. Analogously, Fig. 12(b)

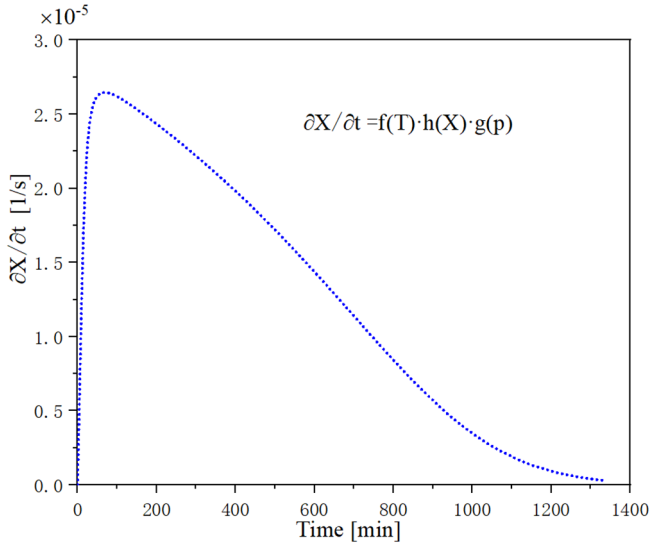


Fig. 8. Reaction kinetics of reaction from hexahydrate to monohydrate.

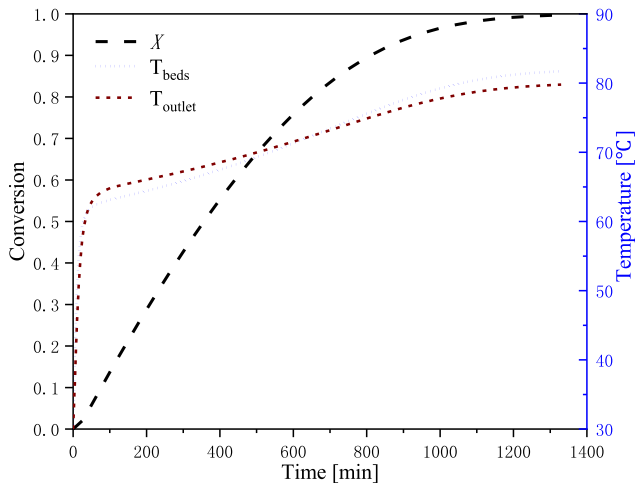


Fig. 9. The average extent of conversion, temperatures of bulk $\text{SrBr}_2 \cdot 6\text{H}_2\text{O}$ and outlet of reactor over time.

indicates that higher inlet velocities lead to faster conversion rates, although higher velocity means more thermal energy is needed to input to the system per unit time in practice.

For discharging, the relative humidity or vapor pressure of the inlet air has a significant influence on hydration. For humid air with a given temperature, the hydration process theoretically improves with a higher moisture content, making it indispensable to humidify the input air when discharging in winter, to further promote the hydration process. Fig. 13(a) reveals that inlet air with a relative humidity of 90% completes the hydration first, when compared with inlet air with a relative humidity of 80%, 70%, or 60%. The time required is ~855 min, 940 min, 1055 min, and 1215 min, respectively. As with the charging process, the increased inlet velocity accelerates the discharging process, as seen in Fig. 13(b). However, with the volume flow rate increase, the temperature of the warm outlet air decreases, and the household heating may subsequently be weakened. Therefore, it is advisable to choose a lower inlet velocity or flow rate to extend the discharging process, to achieve a longer heat release time as well as higher temperatures.

4.3.2. Effect of heat and mass transfer and kinetic factor

For the salt hydrate based TCHS system, an important issue is the

low thermal conductivity of the solid grains, which could restrain the heat transfer. The mass transfer, is likewise restricted due to the low permeability. Therefore, some researchers [38,39,45–47] use salt-hydrates and vermiculite or zeolite to prepare composite sorbents to strengthen the stability and thermal conductivity for thermal energy storage. Fig. 14(a) and (b) depict how the reaction rate slightly increases with the greater thermal conductivity and permeability for a given time. Especially, once λ_s exceeds $2 \text{ W m}^{-1} \text{ K}^{-1}$, or permeability exceeds $5 \times 10^{-11} \text{ m}^2$, the increase of the reaction rate is un conspicuous even if the λ_s or k_p increases, which indicates that the λ_s or k_p is not the main limitation beyond a certain value [44], when other parameters are kept constant at their reference values. For example, the time to reach $X = 0.99$ has a 5.86% (70 min) decrease when λ_s changes from $0.7 \text{ W m}^{-1} \text{ K}^{-1}$ to $2 \text{ W m}^{-1} \text{ K}^{-1}$. After that, increasing λ_s from $2 \text{ W m}^{-1} \text{ K}^{-1}$ to $8 \text{ W m}^{-1} \text{ K}^{-1}$ only results in a 2.22% (25 min) decrease in the reaction time at $X = 0.99$. Therefore, it could be cost efficient to slightly increase the thermal conductivity of the salt grains

The resulting conversions and the bed temperature versus time under different kinetic factor conditions are presented in Fig. 14(c). According to the formula $R_{kin} = A_f \cdot \exp(-E_a/RT)$, the kinetic factor increases with temperature. The greater kinetic factor values clearly result in a faster desorption. A set of values of kinetic factor which corresponding to several specific temperatures are chosen, to investigate the influence of the temperature of reaction salt on the reaction kinetics. The method is based on the assumption that the temperature of the salt is constant, which is similar to the isothermal sorption process. For the case of $R_{kin} = 0.8 \times 10^{-4}$, the ultimate conversion rate (1330 min) is ~45%, far less than that of other cases. Additionally, Fig. 14(c) proves that $R_{kin} = 1.0 \times 10^{-4}$ is a threshold in this model; below it, the kinetics becomes a limiting factor that seriously slows down the reaction, and above it, the kinetics no longer remarkably influences the reaction rate. Moreover, at the beginning of the dehydration, the temperature of reactive bed decreases with the magnified kinetic factor. The phenomenon is then reversed until dehydration is complete. The reason for this reversal is that the desorption process with smaller kinetic factors are relatively more moderate and slower than that of the cases with greater kinetic factors, due to the endothermic reaction, the slower reaction rate causes faster bed temperature increase. Whereas, the greater kinetic factor leads to more severe desorption reaction and accordingly, more heat is consumed to sustain this endothermic reaction. Consequently, the temperature rise of the bed is weakened to some extent though the bed is heated continuously by hot air. As the reaction continues, there are fewer unreacted salt grains remaining for the case with greater kinetic factor, and accordingly, the heat required to maintain the endothermic reaction is decreased, while the influent hot air is the same, as a result, the bed temperature rises slightly faster and the temperature surpasses that of the cases with smaller kinetic factors.

4.4. Optimization of model structure

A physical model of a reactor which can facilitate the solid-gas reaction is of great significance. For this open multilayered reactor, it is crucial to guarantee that the incoming flow fully contacts the reactive salt of each layer. According to the results from the reference case, the upper beds cannot sufficiently contact the inlet air due to the imbalanced flow distribution. As a result, the total required reaction time is greatly prolonged. Optimizing the structure or layout of the beds can promote the solid-gas reaction to some extent.

The conversion distributions at a given time and the time required to complete desorption for each case are displayed in Figs. 15 and 16. With the desorption process as an example, several reactive structures were proposed to explore the structure's influence on charging time. In all cases, the total amount of reactive salt, the width of the bed, and other reference parameters all remained unchanged, and only the length of the bed changed. Because in the upper beds, especially the top

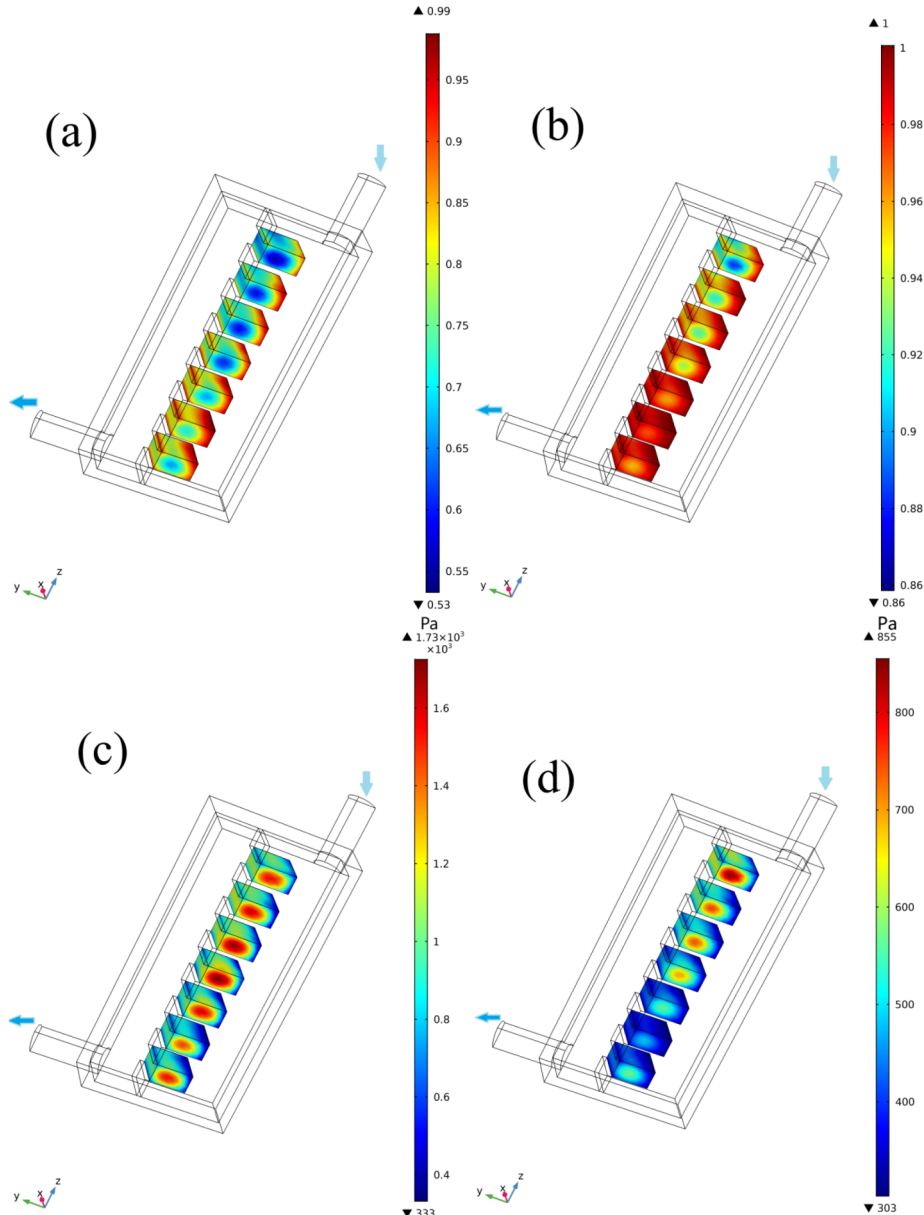


Fig. 10. Conversion distributions of reactive beds at (a) 600 min and (b) 1000 min and vapor pressure at (c) 600 min and (d) 1000 min during charging.

one in the multilayered reactor, complete dehydration is difficult due to the less distributed inlet air, the amount of salt packed in the first bed should be as small as possible. Therefore, two bed configurations were proposed to investigate the influence of the configuration on reaction time. The first configuration was a parabolic form of a symmetric quadratic function; i.e., the middle bed is the longest, and the beds on either side are shorter (Case 1). The second type had a gradually increasing bed length from the top to the bottom (Case 2). The required dehydration time for Case 1 was ~ 1172 min, which is almost as long as the reference case (1180 min); i.e., this configuration did not behave better in time-saving. The dehydration time for Case 2 was ~ 1152 min, which is slightly shorter than the reference case, with only 2.4% time saved. The root cause of this inconspicuous improvement is the low velocity in the reactor and the subsequently weak heat exchange between the fluid and beds. In a new test structure, the space between each reactive bed is shortened from the reference value (2 cm) to 1 cm to decrease the volume of the reactor and further enhance the heat exchange (Case 3). As a result, the time required for dehydration was 1046 min, 11.4% (130 min) shorter than the reference.

4.5. Thermal and exergy performance

The thermal power, efficiency, and coefficient of performance were assessed to further explore the TCHS in the multilayered sieve reactor.

Many formulas have been proposed to determine the charging and discharging power, based on different indicators. For charging, Stitou et al. [48] proposed the following expression for thermal power:

$$P_{ch} = m_{sl} E_{dm} \Delta X / t_{Xch} \quad (20)$$

where E_{dm} and t_{Xch} are the mass energy density and charging time, respectively.

Another universal expression [16] of thermal power for the solid-gas TCHS can be written as follows:

$$P_{ch,V} = \frac{Q_{stor}/V_R}{t_{Xch}} = \frac{(Q_r + Q_{se})/V_R}{t_{Xch}} \quad (21)$$

The first term on the left is the volumetric average thermal power during charging, Q_r is the reaction heat, and Q_{se} is the sensible heat of salt bed and reactor. V_R is the volume of the reactor. Q_r and Q_{se} are

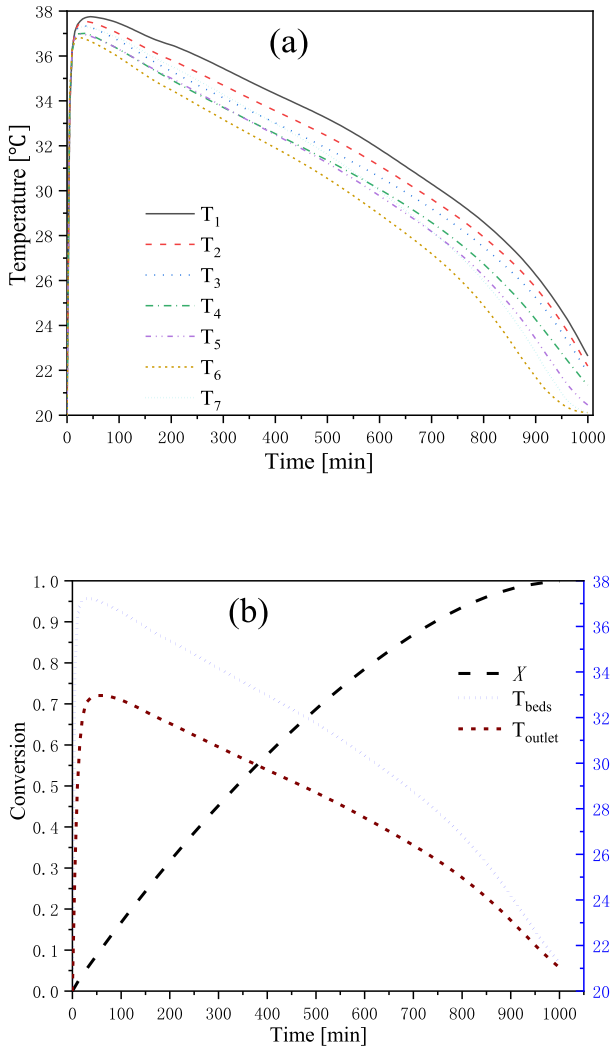


Fig. 11. (a) Temperature of reactive beds vs. time. (b) The average conversion and temperature of bulk $\text{SrBr}_2 \cdot 6\text{H}_2\text{O}$ and outlet of reactor over time during discharging.

defined as follows:

$$Q_r = n \cdot \Delta H = \int (1 - \varepsilon) \frac{\rho_1 X}{M_{s1}} dV \cdot \Delta H_r \quad (22)$$

where n is the amount of salt involved in the reaction, and

$$Q_{se} = Q_{se_salt} + Q_{se_R} + Q_{se_vip} \quad (23)$$

The three terms on the right of Eq. (23) are the sensible heat of salt, the reactor, and the insulating layer, with Q_{se_salt} defined as follows:

$$\begin{aligned} Q_{se_salt} &= m_{s1} C_{ps1} \Delta T + m_{s0} C_{ps0} \Delta T \\ &= \int \rho_{s1} C_{ps1} \Delta T \cdot (1 - X) \cdot (1 - \varepsilon) dV + \int \rho_{s0} C_{ps0} \Delta T \cdot X \cdot (1 - \varepsilon) dV \end{aligned} \quad (24)$$

For discharging, Stitou et al. [48] proposed the average thermal power, concerning both the reaction power and the sensible power developed during the reaction phase as follows:

$$P_{dis} = (1 + \sigma) \left(\frac{\rho_{s0}}{M_{s0}} V_{s0} \Delta H_r \frac{\Delta X}{t_{dis}} \right) \quad (25)$$

where σ represents the energy ratio between the sensible and the reaction energy. Accordingly, the average volume power [16,48] released by the reactive salt can be depicted in the function of the extent of

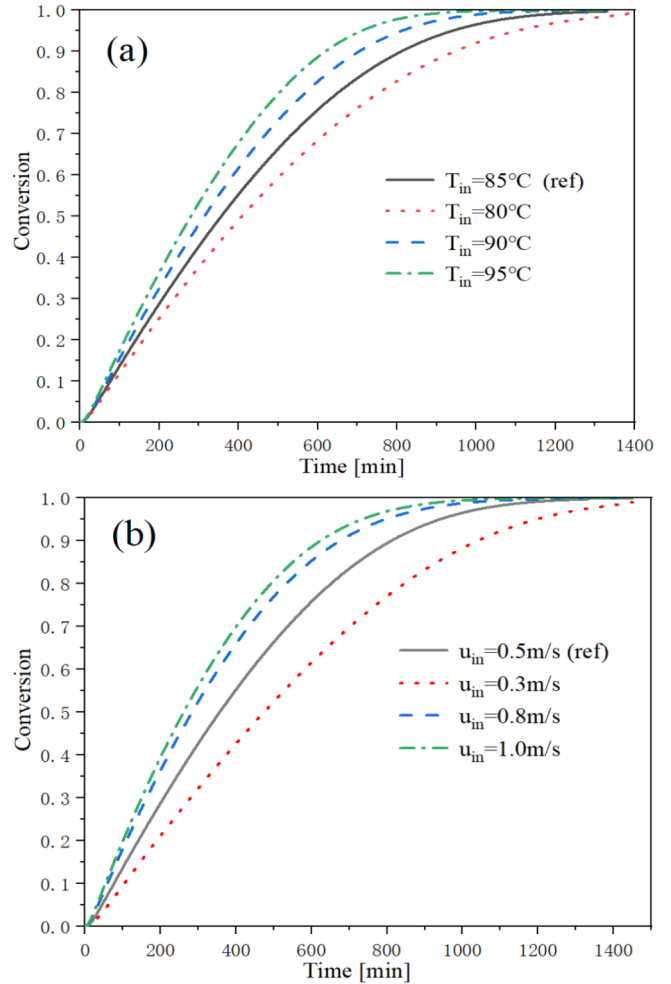


Fig. 12. The conversion evolution with different inlet (a) temperatures and (b) velocities in charging.

conversion:

$$P_{dis_V} = (1 - \varepsilon) \left(\Delta H_r \frac{\rho_{s0}}{M_{s0}} \right) \frac{\Delta X}{t_{dis}} \quad (26)$$

During discharging, the temperatures of air, the salt bed, and the reactor shell all rise due to the exothermic reaction. Thus, the thermal power can also be calculated by the following formula: $P_{dis_V} = \frac{Q_{rele} / V_R}{t_{Xdis}} = \frac{(Q_r - Q_{loss}) / V_R}{t_{Xdis}}$ (27) where Q_{loss} is the heat wasted to the environment, which can be expressed as follows:

$$Q_{loss} = \iint h(T - T_0) dA dt \quad (28)$$

where T_0 is the environmental temperature.

The heat efficiency during charging (dehydration) denotes the ratio of stored heat (reaction heat and sensible heat) to the input heat which is derived from hot air:

$$\eta_{ch} = \frac{Q_{ch,r} + Q_{ch,se}}{H_{ch,in} - H_{ch,out}} \quad (29)$$

where the stored reaction heat of the reactive salt at a given time can be expressed as:

$$Q_{ch,r} = \iint (1 - \varepsilon) \left(\Delta H_r \frac{\rho_{s1}}{M_{s1}} \right) \frac{\partial X}{\partial t} dV dt \quad (30)$$

The heat input to the multilayered sieve reactor is equal to the enthalpy difference between the inlet air and the outlet air, and the air consists of dry air and vapor:

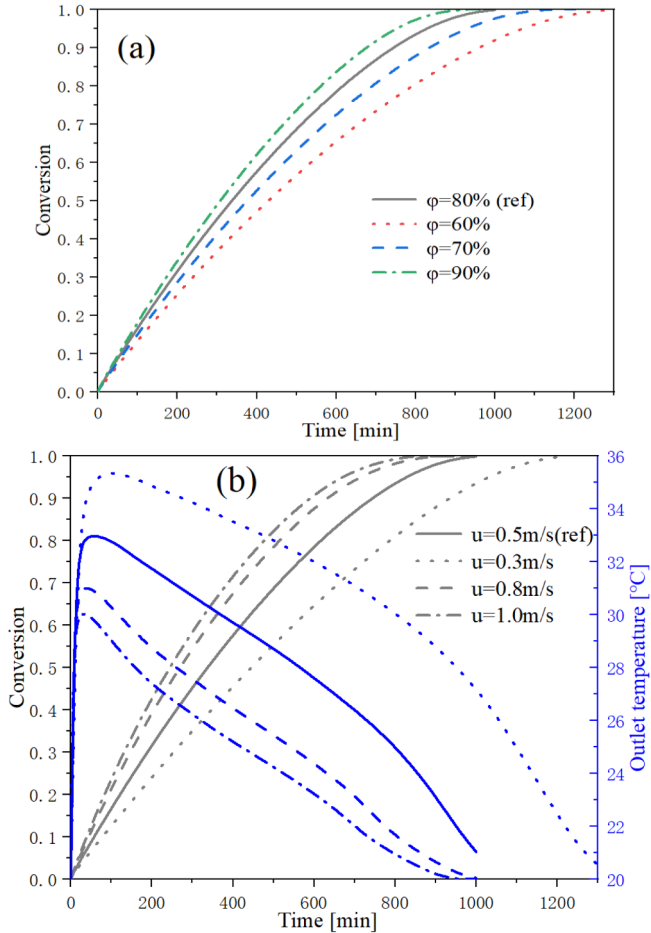


Fig. 13. The conversion evolution with different (a) relative humidities and (b) velocities in discharging.

$$H_{ch,in} = \iint (\rho_{a,ch,in} h_{a,ch,in} + \rho_{v,ch,in} h_{v,ch,in}) v_{n,ch,in} dA dt \quad (31)$$

$$H_{ch,out} = \iint (\rho_{a,ch,out} h_{a,ch,out} + \rho_{v,ch,out} h_{v,ch,out}) v_{n,ch,out} dA dt \quad (32)$$

The heat efficiency of discharging (hydration) is the ratio of the available heat (enthalpy difference + sensible heat due to reaction) to the total heat of sorption.

$$\eta_{dis} = \frac{H_{dis,out} - H_{dis,in} + Q_{dis,se}}{Q_{dis,r}} \quad (33)$$

Likewise, the enthalpy of air can be written as follows:

$$H_{dis,in} = \iint (\rho_{a,dis,in} h_{a,dis,in} + \rho_{v,dis,in} h_{v,dis,in}) v_{n,dis,in} dA dt \quad (34)$$

$$H_{dis,out} = \iint (\rho_{a,dis,out} h_{a,dis,out} + \rho_{v,dis,out} h_{v,dis,out}) v_{n,dis,out} dA dt \quad (35)$$

The thermal coefficient of performance (COP_{th}) and exergy coefficient of performance (COP_{ex}) [47] are used to further analyze system performance, and are defined as follows:

$$COP_{th} = \frac{Q_{out}}{Q_{in}} \quad (36)$$

$$COP_{ex} = \frac{E_{x,out}}{E_{x,in}} = \frac{Q_{out} \left(1 - \frac{T_0}{T_L}\right)}{Q_{in} \left(1 - \frac{T_0}{T_H}\right)} = COP_{th} \left(1 - \frac{T_0}{T_L}\right) \quad (37)$$

$$Q_{out} = H_{dis,out} \quad Q_{in} = H_{ch,in} - H_{ch,out} \quad (38)$$

where T_L is the average outlet temperature during hydration, and T_H is

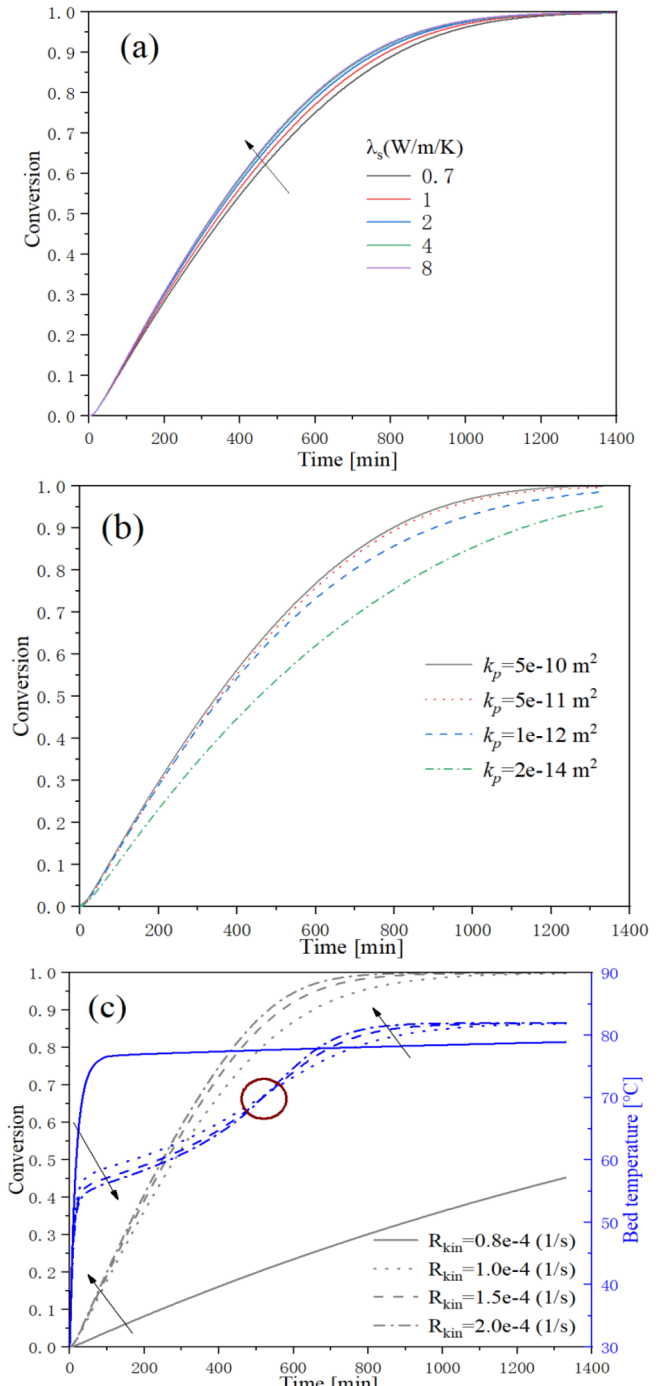


Fig. 14. Influence of (a) the thermal conductivity of the salt, (b) permeability, and (c) reaction kinetic factor on the degree of dehydration.

the inlet temperature during dehydration.

Fig. 17 reveals the thermal power evolution as a function of the reaction conversion during dehydration (charging) and hydration (discharging). During dehydration, the average thermal power decreases from 22 W to 14.3 W between 10% and 99% of reaction conversion, whereas the values does not change much between 10% and 70% of conversion. The thermal power observed in hydration is from 39.1 W to 18.1 W, higher than that of dehydration, which can be attributed to the faster reaction of sorption. On the other hand, the volumetric thermal power of dehydration is greater than that of hydration. The reason is that the sensible heat of the salt and reactor as well as the reaction heat are all provided by the hot air at the inlet during

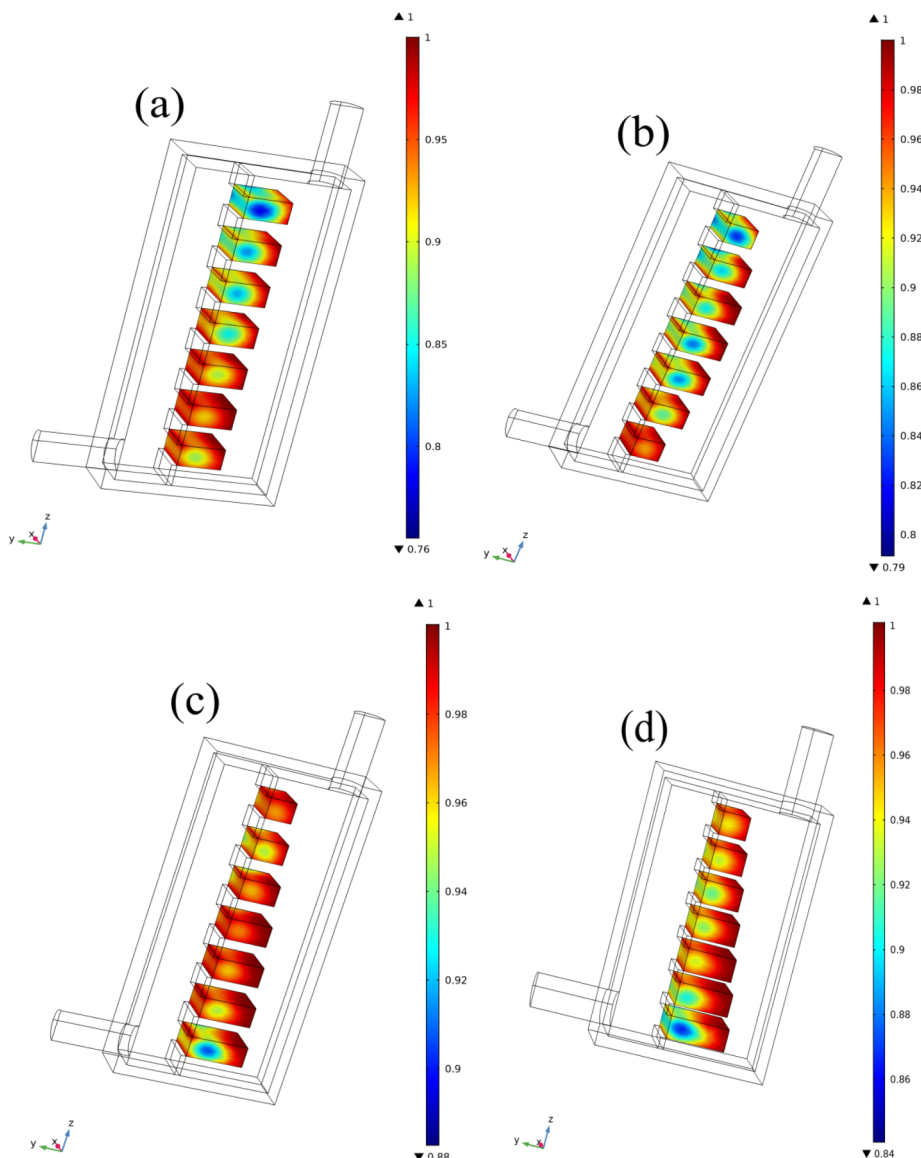


Fig. 15. Conversion degree distributions at 850 min for (a) the reference case, (b) Case 1, (c) Case 2, and (d) Case 3.

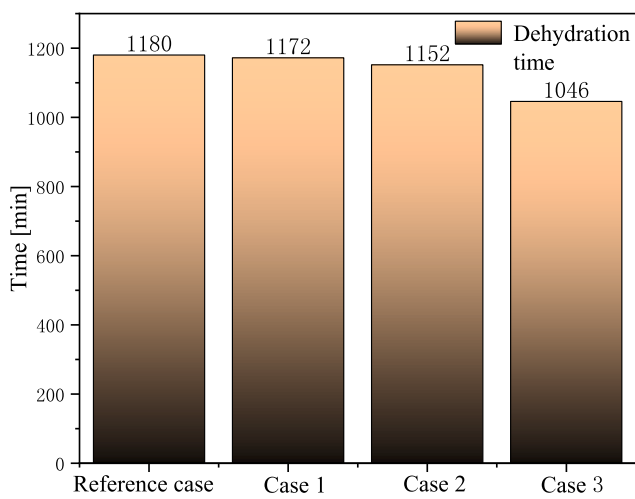


Fig. 16. Required time of dehydration for all cases.

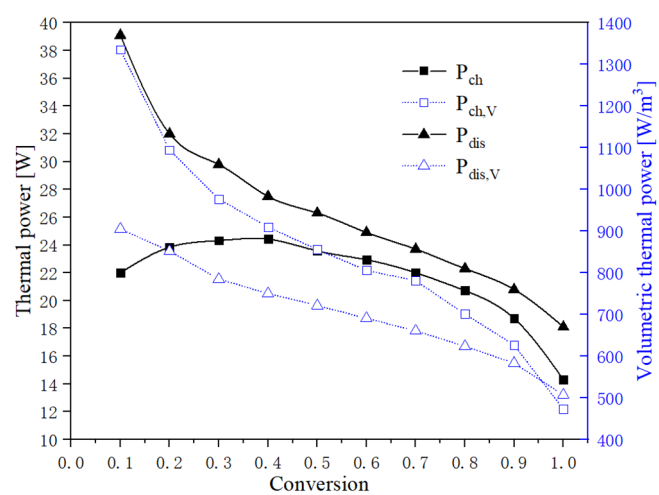


Fig. 17. Evolution of the thermal power.

Table 4a

Evaluation results for different indices in charging.

Indices	Conditions							
	Temperature (°C)				Inlet velocity (m/s)			
	80	85(Ref)	90	95	0.3	0.5(Ref)	0.8	1.0
η_{ch} (%)	81.6	85.2	90.6	91.3	80.0	85.2	86.5	88.8
η_{dis} (%)	94.5	94.5	94.5	94.5	94.5	94.5	94.5	94.5
COP_{th} (%)	70.1	72.4	74.4	76.3	68.5	72.4	73.3	75.1
COP_{ex} (%)	21.8	21.3	21.4	20.4	20.2	21.3	21.6	22.0

Table 4b

Evaluation results for different indices in discharging.

Indices	Conditions							
	Relative humidity (%)				Inlet velocity (m/s)			
	60	70	80 (Ref)	90	0.3	0.5 (Ref)	0.8	1.0
η_{ch} (%)	85.2	85.2	85.2	85.2	85.2	85.2	85.2	85.2
η_{dis} (%)	94.7	94.6	94.5	94.5	91.6	94.5	96.1	96.1
COP_{th} (%)	71.8	71.6	71.5	71.5	69.1	71.5	72.8	72.8
COP_{ex} (%)	19.0	20.1	21.1	22.0	24.2	21.1	18.9	17.9

dehydration, while in hydration, all the heat is derived from the reaction heat, and a part of this heat is lost to the environment.

The thermal efficiency, COP_{th} and COP_{ex} of charging according to Eqs. (29), (36) and (37) are 85.2%, 72.4%, and 21.3%, respectively. Moreover, the corresponding values for discharging are 94.5%, 71.5%, and 21.1%, respectively. Additionally, the detailed results of various operating conditions for charging and discharging are listed in Table 4. The thermal efficiency of charging appears lower than that of discharging, because more heat is lost to the environment due to the relatively higher temperature during charging. The thermal efficiency of charging increases with the temperature of incoming air. Because the time for desorption reaction is shortened due to the higher inlet temperature, although the higher temperature results in greater heat loss, which can be validated by COP_{ex} in Table 4(a). In general, during charging processes with different temperature in this model, the time-shortening effect is more dominant than the heat loss effect. For charging, COP_{th} increases with the input temperature; COP_{ex} decreases basically. Also, both COP_{th} and COP_{ex} increase with the inlet velocity; this result might be attributed to the smaller enthalpy difference between the inlet and outlet hot air for the case of greater inlet velocity. During discharging, on the other hand, COP_{th} tends to decrease with increasing humidity and to increase with inlet velocity roughly, whereas COP_{ex} displays the reverse trend. Table 4 shows that for these given operating conditions, it is difficult to guarantee that all performance indices maintain their best status simultaneously. However, the results can provide some practical guidelines. For example, to achieve the best COP_{ex} , the optimal temperature and inlet velocity of air during charging are 80 °C and 1.0 m/s, respectively and in discharging, the optimal relative humidity and inlet velocity of air are 90% and 0.3 m/s respectively, given that other parameters are kept at reference values.

5. Conclusions

$SrBr_2 \cdot 6H_2O$ based seasonal thermochemical heat storage has been numerically investigated by introducing a multilayered sieve reactor in this work. This research, based on the effect of coupled heat and mass transfer, conducts a series of simulations about the characteristics of salt dehydration and hydration in an open reactor. Based on reference operating condition, the main findings of this study are summarized as follows:

- In the multilayered sieve-plate reactor, the temperature distribution of the reactive salt beds is uneven due to the imbalanced flow distribution. The temperature of the lower salt beds is higher than that of the upper beds during charging whereas the opposite result occurs during discharging.
- In the heat storage process, the temperature of the salt bed rises rapidly at first to store the sensible heat until the temperature of the bulk $SrBr_2 \cdot 6H_2O$ is higher than 60 °C. Above this temperature, the salt hydrate will further dehydrate, and the rate of temperature rise will be restrained owing to the endothermic reaction. The required times to complete the dehydration (charging) and hydration (discharging) reaction are approximately 1180 min and 940 min, respectively.
- Inlet air with a higher initial temperature and velocity facilitate water vapor desorption. Air with a greater relative humidity can promote vapor sorption. Increased velocity does as well, whereas the outlet temperature decreases with greater velocity.
- The reaction rate is not very sensitive to the thermal conductivity and permeability. The reaction kinetic factor $R_{kin} = 1.0 \times 10^{-4}$ is a threshold in this model.
- The configuration of the reactive salt beds that has increasing bed length from the top to the bottom and a shorter distance between beds (Case 3) is most favorable for promoting reaction. A time-saving of 11.4% (130 min) is achieved for dehydration with this configuration when compared to the reference case.
- The average thermal power and volumetric thermal power decrease with the extent of conversion. In addition, the average thermal power of hydration is higher than that of dehydration, while the volumetric thermal power shows the opposite.
- The thermal efficiency η , COP_{th} and COP_{ex} of charging are 85.2%, 72.4%, and 21.3% respectively, and the corresponding values for discharging are 94.5%, 71.5%, and 21.1%, respectively for the present model. The actual situation should be considered to obtain the optimal or expected performance index.

Declaration of Competing Interest

I am the corresponding author (Min Zeng) and declare no conflict of interest of this submission.

Acknowledgements

This present study is supported by the National Natural Science Foundation of China (No. 51776157) and the Foundation for Innovative Research Groups of the National Natural Science Foundation of China (No. 51721004).

References

- Scapino L, Zondag HA, Van Bael J, Diriken J, Rindt CCM. Energy density and storage capacity cost comparison of conceptual solid and liquid sorption seasonal heat storage systems for low-temperature space heating. Renew Sustain Energy Rev 2017;76:1314–31.
- NTsoukpo KE, Liu H, Le Pierrès N, Luo L. A review on long-term sorption solar energy storage. Renew Sustain Energy Rev 2009;13(9):2385–96.
- Michel B, Mazet N, Mauran S, Stitou D, Xu J. Thermochemical process for seasonal storage of solar energy: characterization and modeling of a high density reactive bed. Energy. 2012;47(1):553–63.
- Michel B, Neveu P, Mazet N. Comparison of closed and open thermochemical processes for long-term thermal energy storage applications. Energy. 2014;72:702–16.
- Chen W, Li W, Zhang Y. Analysis of thermal deposition of $MgCl_2 \cdot 6H_2O$ hydrated salt in the sieve-plate reactor for heat storage. Appl Therm Eng 2018;135:95–108.
- Yan T, Wang RZ, Li TX, Wang LW, Fred IT. A review of promising candidate reactions for chemical heat storage. Renew Sustain Energy Rev 2015;43:13–31.
- Yuan Y, Li Y, Duan L, Liu H, Zhao J, Wang Z. $CaO/Ca(OH)_2$ thermochemical heat storage of carbide slag from calcium looping cycles for CO_2 capture. Energy Convers Manage 2018;174:8–19.
- Dai L, Long X-F, Lou B, Wu J. Thermal cycling stability of thermochemical energy storage system $Ca(OH)_2/CaO$. Appl Therm Eng 2018;133:261–8.
- Yan J, Zhao CY, Pan ZH. The effect of CO_2 on $Ca(OH)_2$ and $Mg(OH)_2$.

- thermochemical heat storage systems. *Energy* 2017;124:114–23.
- [10] Mastronardo E, Bonaccorsi L, Kato Y, Piperoopoulos E, Lanza M, Milone C. Strategies for the enhancement of heat storage materials performances for MgO/H₂O/Mg(OH)₂ thermochemical storage system. *Appl Therm Eng* 2017;120:626–34.
- [11] Pan ZH, Zhao CY. Gas-solid thermochemical heat storage reactors for high-temperature applications. *Energy* 2017;130:155–73.
- [12] Bhouri M, Bürger I, Linder M. Feasibility analysis of a novel solid-state H₂ storage reactor concept based on thermochemical heat storage: MgH₂ and Mg(OH)₂ as reference materials. *Int J Hydrogen Energy* 2016;41(45):20549–61.
- [13] Gu R, Ding J, Wang Y, Yuan Q, Wang W, Lu J. Heat transfer and storage performance of steam methane reforming in tubular reactor with focused solar simulator. *Appl Energy* 2019;233–234:789–801.
- [14] Singh A, Tescari S, Lantin G, Agrafiotis C, Roeb M, Sattler C. Solar thermochemical heat storage via the Co₃O₄/CoO looping cycle: storage reactor modelling and experimental validation. *Sol Energy* 2017;144:453–65.
- [15] Aydin D, Casey SP, Riffat S. The latest advancements on thermochemical heat storage systems. *Renew Sustain Energy Rev* 2015;41:356–67.
- [16] Fopah Lele A, Kuznik F, Opel O, Ruck WKL. Performance analysis of a thermochemical based heat storage as an addition to cogeneration systems. *Energy Convers Manage* 2015;106:1327–44.
- [17] Fopah Lele A, Kuznik F, Rammelberg HU, Schmidt T, Ruck WKL. Thermal decomposition kinetic of salt hydrates for heat storage systems. *Appl Energy* 2015;154:447–58.
- [18] Fopah-Lele A, Rohde C, Neumann K, et al. Lab-scale experiment of a closed thermochemical heat storage system including honeycomb heat exchanger. *Energy*. 2016;114:225–38.
- [19] Donkers PAJ, Sögütoglu LC, Huinink HP, Fischer HR, Adan OCG. A review of salt hydrates for seasonal heat storage in domestic applications. *Appl Energy* 2017;199:45–68.
- [20] Scapino L, Zondag HA, Van Bael J, Diriken J, Rindt CC. Sorption heat storage for long-term low-temperature applications: a review on the advancements at material and prototype scale. *Appl Energy* 2017;190:920–48.
- [21] N'Tsoukpo KE, Schmidt T, Rammelberg HU, Watts BA, Ruck WKL. A systematic multi-step screening of numerous salt hydrates for low temperature thermochemical energy storage. *Appl Energy* 2014;124:1–16.
- [22] Kubota M, Matsumoto S, Matsuda H. Enhancement of hydration rate of LiOH by combining with mesoporous carbon for Low-temperature chemical heat storage. *Appl Therm Eng* 2019;150:858–63.
- [23] Brancato V, Calabrese L, Palomba V, et al. MgSO₄·7H₂O filled macro cellular foams: an innovative composite sorbent for thermo-chemical energy storage applications for solar buildings. *Sol Energy* 2018;173:1278–86.
- [24] Van Essen VM, Zondag HA, Cot Gores J, et al. Characterization of MgSO₄ Hydrate for Thermochemical Seasonal Heat Storage. *J Sol Energy Eng* 2009;131(4):514–24.
- [25] Zondag H, Kikkert B, Smeding S, Boer Rd, Bakker M. Prototype thermochemical heat storage with open reactor system. *Appl Energy* 2013;109:360–5.
- [26] Ferchaud C, Zondag H, Veldhuis J, et al. Study of the reversible water vapour sorption process of MgSO₄·7H₂O and MgCl₂·6H₂O under the conditions of seasonal heat storage. *J. Phys. – Conf. Ser.* 2012;395:012–69.
- [27] Gaeini M, Rouws AL, Salar JWO, Zondag HA, Rindt CCM. Characterization of microencapsulated and impregnated porous host materials based on calcium chloride for thermochemical energy storage. *Appl Energy* 2018;212:1165–77.
- [28] Mamani V, Gutiérrez A, Ushak S. Development of low-cost inorganic salt hydrate as a thermochemical energy storage material. *Sol Energy Mater Sol Cells* 2018;176:346–56.
- [29] Sutton R, Jewell E, Searle J, Elvins J. Discharge performance of blended salt in matrix materials for low enthalpy thermochemical storage. *Appl Therm Eng*
- 2018;145:483–93.
- [30] Sutton RJ, Jewell E, Elvins J, Searle JR, Jones P. Characterising the discharge cycle of CaCl₂ and LiNO₃ hydrated salts within a vermiculite composite scaffold for thermochemical storage. *Energy Build* 2018;162:109–20.
- [31] Farcot L, Le Pierrès N, Michel B, Fourmigué J-F, Papillon P. Numerical investigations of a continuous thermochemical heat storage reactor. *J Energy Storage* 2018;20:109–19.
- [32] Wyttensbach J, Bougard J, Descy G, et al. Performances and modelling of a circular moving bed thermochemical reactor for seasonal storage. *Appl Energy* 2018;230:803–15.
- [33] Mallez-Ernewein A, Lorente S. Constructal design of thermochemical energy storage. *Int J Heat Mass Transf* 2019;130:1299–306.
- [34] Maria F, Neveu P, Tanguy G, Papillon P. Thermodynamic analysis and experimental study of solid/gas reactor operating in open mode. *Energy* 2014;66:757–65.
- [35] Fopah-Lele A, Tamba JG. A review on the use of SrBr 2·6H₂O as a potential material for low temperature energy storage systems and building applications. *Sol Energy Mater Sol Cells* 2017;164:175–87.
- [36] Michel B, Mazet N, Neveu P. Experimental investigation of an innovative thermochemical process operating with a hydrate salt and moist air for thermal storage of solar energy: global performance. *Appl Energy* 2014;129:177–86.
- [37] Michel B, Mazet N, Neveu P. Experimental investigation of an open thermochemical process operating with a hydrate salt for thermal storage of solar energy: local reactive bed evolution. *Appl Energy* 2016;180:234–44.
- [38] Zhao YJ, Wang RZ, Zhang YN, Yu N. Development of SrBr 2 composite sorbents for a sorption thermal energy storage system to store low-temperature heat. *Energy* 2016;115:129–39.
- [39] Zhang YN, Wang RZ, Zhao YJ, Li TX, Riffat SB, Wajid NM. Development and thermochemical characterizations of vermiculite/SrBr 2 composite sorbents for low-temperature heat storage. *Energy* 2016;115:120–8.
- [40] Courbon E, D'Ans P, Permyakova A, et al. A new composite sorbent based on SrBr 2 and silica gel for solar energy storage application with high energy storage density and stability. *Appl Energy* 2017;190:1184–94.
- [41] Olives R, Mauran S. A highly conductive porous medium for solid–gas reactions: effect of the dispersed phase on the thermal tortuosity. *Transp Porous Media* 2001;43(2):377–94.
- [42] Esaki T, Kobayashi N. Reaction rate characteristics of SrBr 2 hydration system for chemical heat pump cooling mode. *J Mater Sci Chem Eng* 2016;4:106–15.
- [43] Fopah Lele A. Thermochemical heat storage system for households: thermal transfers coupled to chemical reaction investigations [Doctorate/Ph.D.]. Leuphana University of Lüneburg; 2015.
- [44] Ferchaud CJ, Zondag H, Rubino A, et al. Seasonal sorption heat storage – Research on thermochemical materials and storage performance. *Heat Powered Cycles*. The Netherlands; 2012.
- [45] Casey SP, Aydin D, Elvins J, Riffat S. Salt impregnated desiccant matrices for 'open' thermochemical energy conversion and storage – Improving energy density utilisation through hydrodynamic & thermodynamic reactor design. *Energy Convers Manage* 2017;142:426–40.
- [46] Xu SZ, Lemington, Wang RZ, et al. A zeolite 13X/magnesium sulfate–water sorption thermal energy storage device for domestic heating. *Energy Convers Manage* 2018;171:98–109.
- [47] Xue B, Ye S, Zhang L, Wei X, Nakaso K, Fukai J. High-temperature steam generation from low-grade waste heat from an adsorptive heat transformer with composite zeolite-13X/CaCl₂. *Energy Convers Manage* 2019;186:93–102.
- [48] Stitou D, Goetz V, Spinner B. A new analytical model for solid-gas thermochemical reactors based on thermophysical properties of the reactive medium. *Chem Eng Process* 1997;36:29–43.